Author/s:
Sindram, J;Volk, K;Mulvaney, P;Karg, M

Title:
Silver Nanoparticle Gradient Arrays: Fluorescence Enhancement of Organic Dyes

Date:
2019-07-02

Citation:
Sindram, J., Volk, K., Mulvaney, P. & Karg, M. (2019). Silver Nanoparticle Gradient Arrays: Fluorescence Enhancement of Organic Dyes. Langmuir, 35 (26), pp.8776-8783. https://doi.org/10.1021/acs.langmuir.9b01027.

Persistent Link:
https://hdl.handle.net/11343/345852

Silver Nanoparticle Gradient Arrays: Fluorescence Enhancement of Organic Dyes

Julian Sindram,[a] Kirsten Volk,[a] Paul Mulvaney,[b] and Matthias Karg[a*]

[a] Institut für Physikalische Chemie I: Kolloide und Nanooptik, Heinrich-Heine-Universität Düsseldorf,
Universitätsstraße 1, D-40225 Düsseldorf, Germany.

[b] ARC Centre of Excellence in Exciton Science, School of Chemistry,
Parkville, VIC., 3010, Australia.

*karg@hhu.de

Abstract

Noble metal nanoparticles show pronounced extinction peaks in the visible wavelength range due to their localized surface plasmon resonances. The excitation of these resonances leads to strong confinement of electromagnetic energy at nanometer scales, which is critical for ultrasensitive, fluorescence based detection of analytes. The strength and spatial distribution of this near-field zone depends on particle size, shape and composition. To determine how these near-field effects depend on the particle size, we have prepared nanoparticle gradients on centimeter-scale substrates using a colloid-based approach. This plasmonic gradient is used to study the steady-state emission and fluorescence lifetime of a common organic dye that was embedded into the monolayer.

Keywords

Silver nanoparticle monolayer, localized surface plasmon resonance, near-field enhancement, particle size gradient, core/shell microgels

Introduction

Noble metal nanoparticles such as silver and gold exhibit localized surface plasmon resonances (LSPRs) due to the collective excitation of the conduction electrons by an incident electromagnetic wave.[1] For spherical particles with sizes below 100 nm, these resonances correspond typically to dipolar modes. The resonance position and strength directly depend on the particle size,[2, 3, 4, 5] the dielectric environment,[6, 7, 8, 9] and the inter-particle spacing.[2, 6, 10, 11] While the optical response of small nanoparticles is dominated by absorption, the scattering contribution increases with increasing particle size.[4] Nanostructures that support LSPRs are interesting for a variety of applications such as light management in thin-film solar cells,[12, 13, 14] sensing as in the case of Surface Enhanced Raman Scattering (SERS)[15, 16] and plasmonic nanolasers, e.g. from periodic particle arrays.[17] These applications capitalize on the fact that the LSPR excitation leads to the strong nanoscale concentration of electromagnetic energy.[3, 18] The electric field strength at the particle surface can exceed the incident field strength by several orders of magnitude. Both the field enhancement factor and the near-field range, i.e. the distance from the surface at which significant enhancement is observed, increase with particle size.[19] Over the last few years several protocols for the wet-chemical synthesis of gold[20, 21] and silver[22, 23] nanoparticles with excellent size control and narrow polydispersity have been reported. These approaches however lead to individual batches of nanoparticles with distinct particle sizes which makes rapid testing of size dependent phenomena slow and laborious. Furthermore, it is easier to implement such particle based tests on solid supports. Challenges that have to be addressed when transferring nanoparticles synthesized in dispersion onto solid substrates are the control over inter-particle spacing and the prevention of particle aggregation. A useful way to simultaneously enhance the colloidal stability of noble metal nanoparticles and to control inter-particle spacing during assembly on a substrate is through

the use of polymeric ligands[24, 25] or encapsulation in hydrogels.[11, 26] For such core/shell systems the polymer shell thickness controls the separation between particles, i.e. thicker shells result in larger separations. Müller et al. have demonstrated that gold nanoparticles encapsulated in hydrogel shells composed of cross-linked poly(*N*-isopropylacrylamide) (PNIPAM) can be used for the preparation of a gold nanoparticle monolayer on cm^2-scale areas with well-defined, large inter-particle spacings.[27] These non-close-packed monolayers were then used to prepare a linear gradient in gold nanoparticle size using a seeded-growth protocol with the initial gold cores acting as seeds.

In this work we prepare a monolayer of non-close-packed, spherical gold nanoparticles (AuNPs) by spin-coating Au-PNIPAM core/shell microgels onto glass substrates and then overgrowing the seeds with silver. We have developed a synthesis that allows the spherical morphology and low polydispersity of the initial seeds to be maintained while preventing secondary nucleation. The reaction time can be used to precisely control the thickness of the silver shells. **Scheme 1** illustrates the structure of the core/shell microgels and the fundamental steps of the gradient preparation. We have studied the emission of Atto 488, an organic dye, placed in the nearby environment. We demonstrate continuous enhancement of the dye emission for increasing particle size, i.e. for increasing near-field strength and a shorter lifetime along the gradient, proving that the gradients act as an efficient platform for optimization of near-field interactions.

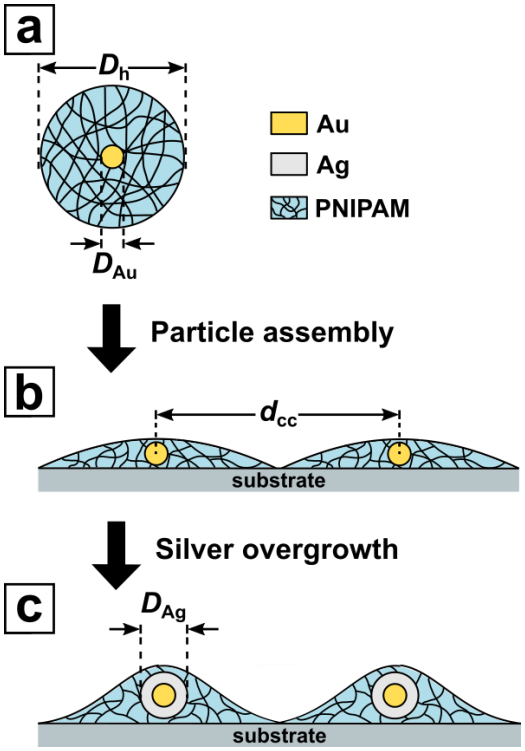

Scheme 1: Illustration of the fundamental steps involved in the preparation of silver gradients and the relevant structural parameters of the system. The core/shell microgels **(a)** comprise a small gold core with diameter D_{Au} and a cross-linked PNIPAM hydrogel shell, which is strongly swollen with water. The overall hydrodynamic diameter of the core/shell microgels is D_h. The particles are assembled on a solid substrate by spin coating **(b)** yielding a particle monolayer with a nearest neighbor inter-particle distance d_{cc}. Due to particle deformation d_{cc} is larger than the hydrodynamic diameter D_h in dispersion. During the seed-mediated overgrowth in the last step **(c)**, a silver shell is deposited onto the gold particles and the diameter of the metal core increases from D_{Au} to D_{Ag}.

Results & Discussion

Colloidal building blocks and monolayer preparation. Au-PNIPAM core/shell particles with spherical gold nanoparticle cores and thick PNIPAM hydrogel shells were synthesized by seeded precipitation polymerization.[26] The PNIPAM shell fulfills several purposes during the assembly of the nanoparticle monolayers. Firstly, it acts as a spacer, keeping the plasmonic cores at a sufficient separation to avoid plasmon resonance coupling via near-field interaction. Secondly, the softness of the hydrogel shells promotes the formation of homogeneous, ordered monolayers. Thirdly, the strong adhesion between

the shell and substrate ensures the immobilization of the particle monolayer on the substrate. **Figure S1** in the Supporting Information shows representative TEM images of the AuNP cores and the Au-PNIPAM core/shell microgels. The images reveal the low polydispersity of the cores as well as the successful encapsulation in PNIPAM shells. The wavelength of the LSPR maximum of the as-prepared AuNP cores is 518 nm. After encapsulation in the PNIPAM shell, the LSPR is red-shifted to 524 nm due to the increased refractive index (RI). As the polymer is strongly swollen with water, the effective refractive index near the AuNP surface (approximately 1.36) is only slightly larger than the refractive index of water and, thus, the red-shift is rather small. [28] The respective spectra can be found in the Supporting Information, **Figure S1c**.

The core/shell microgels are monodisperse with a mean hydrodynamic diameter of $\overline{D}_h = 214$ nm in the swollen state (25°C) as determined by dynamic light scattering (see **Figure S2** in the Supporting Information).

Monolayers of Au-PNIPAM core/shell microgels were prepared by spin-coating from a 0.25 wt% dispersion in water, using 76 mm × 26 mm microscopy glass slides as substrates. A homogeneous particle number density was realized using a recessed chuck and an optimized speed ramp (see Supporting Information, **Figure S3**). **Figures 1 (a) – (c)** show AFM height images measured at different positions on the substrate which are indicated in the digital photograph of the final gradient sample in **Figure 1 (g)**. AFM images and their analysis for all sample positions, A-F, are provided in the Supporting Information, **Table S1** and **Figure S4**. The grey insets in the AFM images of **Figure 1** are FFTs of the corresponding scans. The particles form a complete monolayer with hexagonal order and relatively small domain sizes of 5 – 25 μm^2. Point and line defects restrict the domain size of the monolayer. The FFT of the scan near the center of the substrate (posi-

tion C) shows segmented arcs rather than closed Debye-Scherrer rings, indicating a preferential orientation of the domains in this area. As the domain size decreases towards the edges of the substrate, they become more randomly oriented and the features in the FFTs are smeared out. Nevertheless, the local hexagonal ordering and mean inter-particle distance remain unaltered. This is further demonstrated by the pair-correlation functions $g(r)$ shown in **Figure 1 (d) – (f)**. These plots illustrate the relative probability of finding a second particle at a given distance from a chosen center particle, averaged over all the particles in the scan. The first peak in $g(r)$ corresponds to the nearest neighbor center-to-center distance d_{cc}, which was extracted from the data using a Gaussian fit. The dotted, vertical lines in the $g(r)$ plots indicate the mean value of d_{cc} again averaged over the entire AFM scan of the substrate. **Figure 1 (h)** shows the number of particles per surface area, σ, as a function of the position on the substrate. Values of σ were obtained by dividing the counted particle number per scan by the scan area, i.e. 30 µm × 30 µm. The dotted, horizontal line indicates the mean value of σ from all scans measured on the substrate. The grey area represents the standard deviation, which was calculated from the variance of d_{cc} using geometrical considerations (see Supporting Information for more details). For this particular sample we found a mean nearest neighbor distance $d_{cc} = 320 \pm 14$ nm and a mean particle number density $\sigma = 11.3 \pm 1.0$ µm^{-2}.

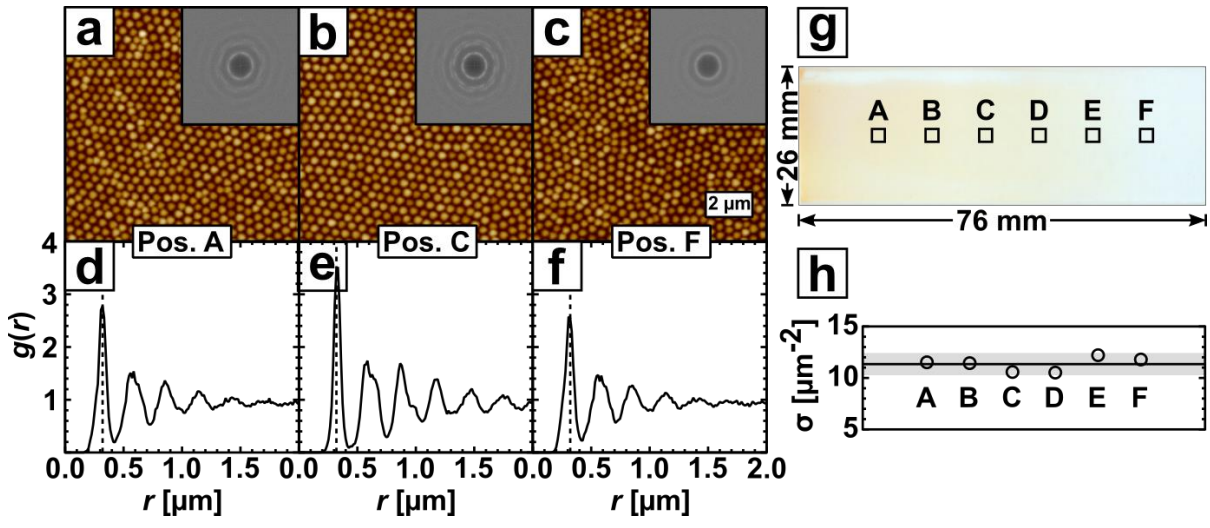

Fig. 1: (a) – **(c)** AFM height images of Au-PNIPAM colloidal monolayers measured at different substrate positions. The insets are FFTs of the corresponding particle position maps. **(d)** – **(f)** Pair-correlation functions *g(r)* generated from x-y-position data. The dotted, vertical lines mark the average nearest neighbor distance d_{cc} for all positions measured on the substrate. **(g)** Photograph of a silver particle size gradient on a substrate. The boxes mark the positions at which AFM/SEM measurements were performed (not to scale). **(h)** Particle number density σ obtained from the AFM images. The dotted, horizontal line marks the average σ and the grey area corresponds to the standard deviation calculated from the variance of d_{cc}.

Preparation and characterization of plasmonic gradients. The substrate-supported monolayer of Au-PNIPAM core/shell microgels featuring well-spaced AuNP cores can be used to prepare a linear gradient in particle size. The preparation procedure is based on seed-mediated overgrowth of the small AuNP cores by silver. To achieve this, the substrate carrying the monolayer is immersed in a growth solution. The immersion time is used to control the growth. By slowly retracting the substrate from the growth solution, a plasmonic gradient is created. Each position along the substrate represents a different immersion time and therefore comprises NPs with different diameters. Although there are several protocols for the seed-mediated growth of silver in a dispersed phase, transferring these methods to substrate-supported particle systems is challenging. The stability of Ag^+ ions in solution strongly depends on pH and coordination environment and silver metal can readily deposit on various surfaces. Moreover, Ag^+ ions are prone to photoreduction in the presence of electron donors.[29] Sánchez-Iglesias et al. have overgrown small substrate-supported AuNP seeds with a silver shell using hydroquinone as reducing agent.[30] However, this reaction system is sensitive to impurities and light. Moreover, side reactions related to the presence of our PNIPAM shell may occur. Consequently, we have developed a new growth protocol that is explained in the Experimental Section in detail. With our protocol we achieve a slow and continuous seed-mediated growth without sec-

ondary nucleation or non-specific silver deposition. By fine-tuning the reaction conditions, the spherical shape is maintained throughout the process. Our overgrowth protocol is carried out in a mixture of ethanol and water with an ethanol volume fraction of 55% as bulk solvent, which has been cooled to 0 °C. Under these conditions, the stability against photo-reduction and secondary nucleation is greatly improved and the growth rate is reduced compared to aqueous systems. The growth solution contains glycine as buffer. Silver nitrate and ascorbic acid are subsequently added and the substrate is immersed to start the growth process. More information on the growth conditions can be found in the Experimental Section and the Supporting Information (e.g. **Table S2**). In order to achieve a particle size gradient, the substrate is slowly withdrawn from the solution. During the 60 minutes it takes to fully retract the substrate, growth proceeds only on the immersed areas. **Figure 2** shows the results from the characterization of a plasmonic Ag@AuNP gradient by SEM and UV-Vis absorbance spectroscopy in dependence of the corresponding position on the substrate. The digital photograph **(a)** shows the substrate carrying the plasmonic gradient. From left to right, the intensity of the yellow coloration, caused by the LSPR of the Ag@AuNPs, increases. Additionally, the color changes from a very bright yellow on the left towards almost orange on the far right edge of the substrate. The color-coded boxes mark the positions where SEM measurements have been performed. Representative images from the corresponding positions are shown in **(b)** – **(f)**. From left to right, an increase in the diameters of the Ag@Au cores (bright spots) can be seen. The PNIPAM shells can be depicted as the dark gray corona homogeneously surrounding the high contrast metal cores. The SEM images also demonstrate the absence of non-spherical core morphologies, such as rods or triangles. Using image analysis, the core diameter has been extracted for each position on the substrate. The corresponding size histograms and Gaussian fits to the distributions are shown in the graph in panel **(g)**. Along the substrate,

the maximum of the size distribution shifts towards larger diameters. The width of the size distribution initially increases and starts to level off at a value around ΔD_{Ag} = ± 8.5 nm after 15 minutes. Panel **(h)** shows the corresponding UV-Vis absorbance spectra measured at each position. With increasing Ag@Au core size, the absorbance at the LSPR becomes stronger and the absorbance maximum red-shifts as expected for increasing particle size.[5, 27] All sample positions reveal single LSPR peaks related to single dipolar modes. The absence of other peaks or distinct shoulders confirms the predominantly spherical shape of the overgrown particles.

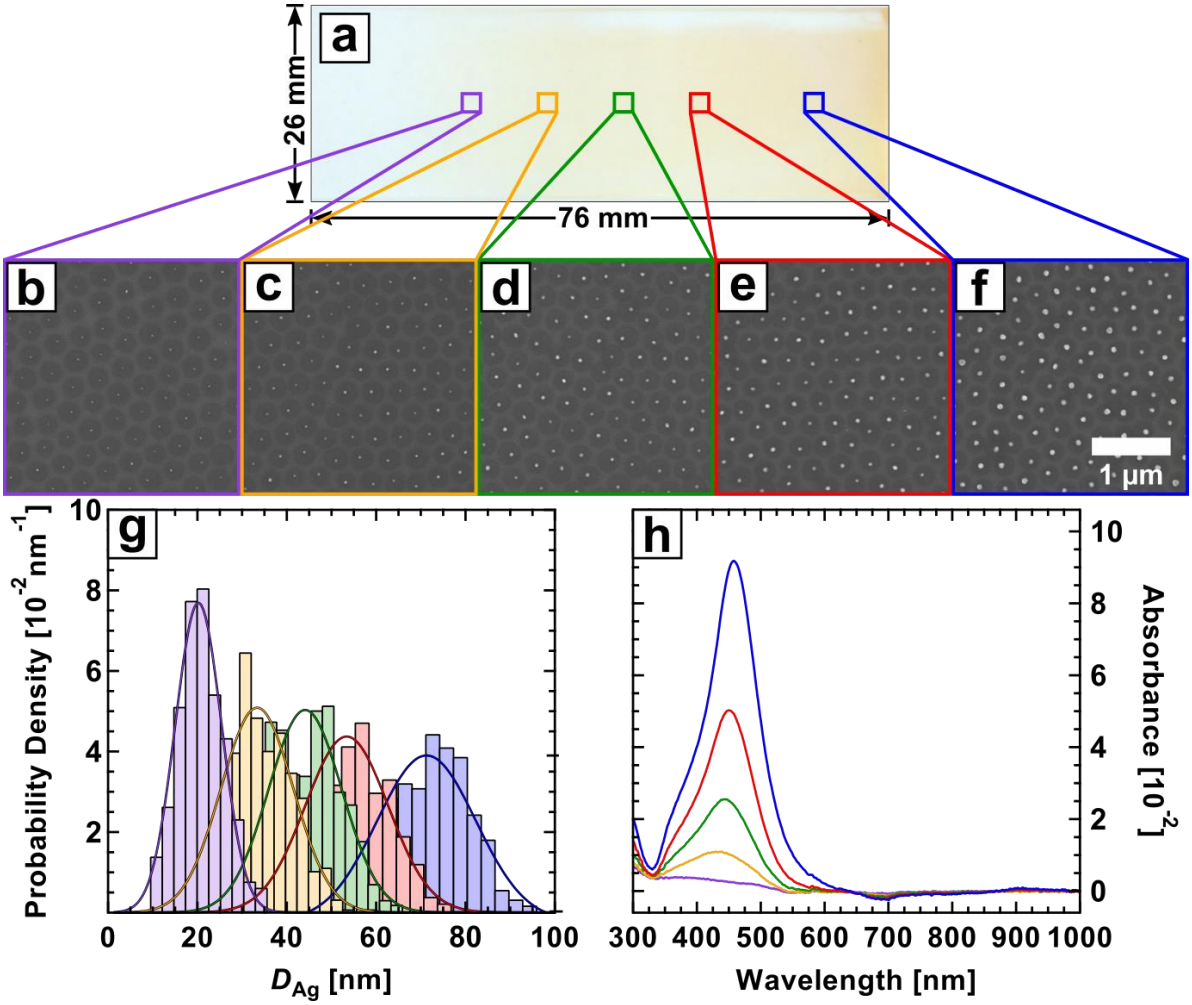

Fig. 2: Characterization of Ag@AuNP size gradients on a single substrate. **(a)** Digital photograph of the plasmonic gradient, showing the yellow coloring from the Ag@AuNPs grown on the substrate. **(b)** – **(f)** SEM images measured at the positions marked in the photograph, showing the Ag@Au cores (bright spots) and the collapsed hydrogel shell (dark grey coronas). **(g)** Histograms showing the distribution of core particle diameters determined from the SEM images. The solid lines are Gaussian

fits to the individual histograms. **(h)** UV-Vis spectra measured at the sample positions highlighted in **(a)**.

The evolution of the mean diameter D_{Ag} and the size distribution during the growth are summarized in **Figure 3 (a)**. After an induction phase of 10 – 15 min, the diameter increases steadily for at least 30 min. At immersion times over 50 min, the growth rate seems to slow down, possibly due to depletion of Ag^+ ions. This nearly linear size increase with time differs significantly from the diffusion-limited growth kinetics found for AuNP gradients by Müller et al.[27]

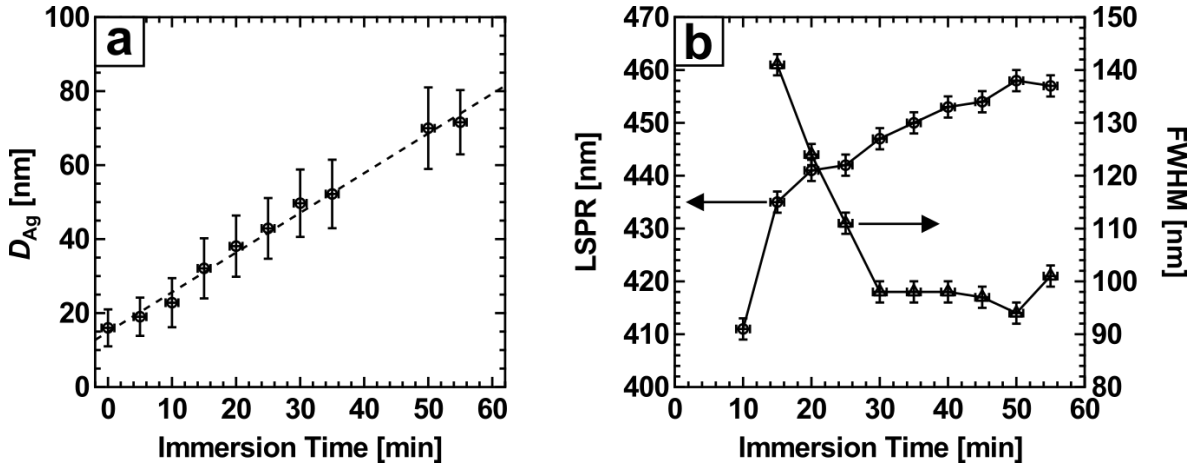

Fig 3: (a) Increase in the silver particle diameter determined from SEM images as a function of the immersion time. The dashed line is a linear fit to the data. **(b)** Change in the LSPR peak position and FWHM as a function of the immersion time.

Figure 3 b summarizes the changes of the optical properties across the substrate, i.e. with increasing immersion time. As the silver shell grows the LSPR emerges – first at approx. 410 nm wavelength – and then red-shifts with increasing D_{Ag}. The full width at half maximum (FWHM) of the LSPR steadily decreases starting from 140 nm until particle diameters of 50 nm are reached and then levels off at a value just below 100 nm. Since the LSPR maximum continues to red-shift during the entire growth process, the mode quality factor $Q = \lambda_{LSPR}/FWHM_{LSPR}$ increases (see **Figure S5**). This effective line narrowing differs from the behavior usually observed for AgNPs in aqueous dispersion, where the LSPR tends to broaden with increasing particles size.[22] In our case, the inter-particle distance is

short enough to allow weak dipole coupling between the LSPRs of the larger particles towards the end of the growth process.[11] The coupling increases the relaxation time of the plasmon resonance and causes the observed narrowing of the LSPR. However, the coupling strength is limited by the inhomogeneous refractive index environment surrounding the particles.[9] Moreover, the plasmonic contribution of the small AuNP core is not negligible for particles with a relatively thin Ag shell.[5] Although the volume fraction of silver quickly approaches 100%, the core/shell structure of the particles can significantly change the optical response. For example, an Ag@Au core/shell particle with gold core diameter of $D_{Au} = 15$ nm and a silver shell thickness $\delta_{Ag} = 2$ nm has a 50:50 volume ratio of the two metals. At $\delta_{Ag} = 9$ nm the volume fraction of silver already exceeds 90%. As the surface plasmon wavelength of gold and silver nanoparticles differs by roughly 100 nm and the optical response of core/shell particles comprises features of both metals, the LSPR of the smaller Ag@Au particles is broader than that of a pure AgNP of the same size.

Fluorescence enhancement in plasmonic gradients. With the increasing LSPR strength for increasing particle sizes along our linear gradient sample, we expect the strength and spatial range of the near-field zone to increase. To probe the near-field, we use the fluorescence of the organic dye Atto 488. With this approach we capitalize on the fact that plasmonic near-fields can enhance the rate at which a fluorophore is excited, thus increasing the emission intensity.[19, 31, 32]

Conveniently our plasmonic nanoparticles of the gradient sample are encapsulated in PNIPAM shells that can be used for infiltration of the dye. To do so the gradient sample is covered with a layer of the dye dissolved in DMSO that swells the PNIPAM shells and enables diffusion of the dye into the shells. Thus, the dye is expected to be homogeneously

distributed within the hydrogel shells across the whole substrate, irrespective of the size of the core particle. The residual liquid is then removed to obtain the dry, dye-loaded plasmonic gradient. The emission spectra shown in **Figure 4 (a)** confirm that dye is successfully incorporated in the plasmonic gradient. The spectra have been measured at different positions on the substrate and are labelled according to the diameter of the Ag@Au particles at each position. The emission spectra show single peaks with maxima at approximately 527 nm, slightly red-shifted compared to the reference value of 520 nm of Atto 488 dissolved in PBS buffer. This difference in emission wavelength is due to the difference in dielectric properties of the medium. The line shape and linewidth do not change along the gradient but the emission intensity is enhanced with increasing Ag@AuNP diameter. Comparing the emission for a particle diameter of 19 nm with the largest studied diameter of 70 nm, an emission enhancement by more than a factor of three is observed. This effect is clearly related to the increasing near-field with increasing particle size. In addition to steady-state fluorescence spectra, we have also measured the fluorescence lifetimes of the dye at different positions along the gradient. **Figure 4 (b)** shows the relative emission intensities as a function of decay time for the different particle diameters.

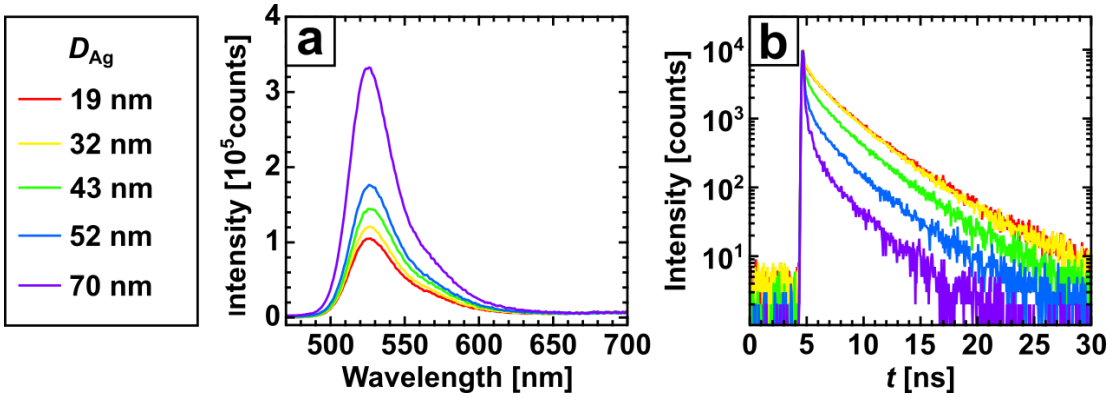

Fig 4: **(a)** Emission spectra measured on the plasmonic gradient after infiltration with Atto 488. The individual spectra are indicated by the corresponding particle sizes at the measured positions. **(b)** Fluorescence lifetime decay curves measured at the same positions on the substrate.

The emission decay curves exhibit pronounced deviations from the ideal single-exponential decay usually found for fluorescent dyes. For large D_{Ag} there is a steep decline in intensity within the first 2 ns after excitation. This is a strong indication of a fast decay pathway emerging with increasing particle size. The data are analyzed using a model comprising two stretched exponential components. More details on the fitting models and the obtained fit parameter are provided in the Supporting Information. In our case, the stretch parameter β reflects the spatial and orientational distribution of dye molecules in the polymer matrix, leading to a distribution of decay rates. The bi-exponential fit reveals a very fast decay pathway with τ_1 << 10 ps which is present in all measurements and which becomes more dominant with increasing particle size. Such short lifetimes are typical for non-radiative processes. As the lifetime of this component is below the instrument resolution, it could not be accurately determined and resulted in large fitting errors. A steady decrease in fluorescence lifetime with increasing particle diameter is observed for the second, slower decay component. The measured range of τ_2 is from 1.94 ns for the smallest particles to 0.52 ns for the largest values of D_{Ag}. A reference sample prepared using SiO_2-PNIPAM core/shell microgels (**Figure S6** in the Supporting Information) instead of plasmonic core particles yields a lifetime of τ_2 = 2.2 ns. As these lifetimes are short compared to the lifetime of 4.1 ns for Atto 488 in bulk solution there seems to be an intrinsic effect of the dye infiltration procedure on fluorescence lifetimes. A second reference sample infiltrated with a reduced dye concentration exhibits a slightly longer lifetime of 2.9 ns. Therefore, self-quenching of the dye by Förster resonance energy-transfer (FRET) is possible (see Supporting Information for additional details).

A plot of the rate of the radiative decay as a function of the emission intensity I_{em} is shown in **Figure 5**. Here, the rate of radiative decay $k_2 = {\tau_2}^{-1}$ is plotted against the emission intensity, normalized to the intensity measured at the sample position with the smallest

particle size. At this position we expect the weakest interaction between the fluorophore and the plasmonic particle. We find that the dye emission increases in intensity while the lifetime becomes shorter. As demonstrated by a linear fit to the data (slope = 0.505 ns^{-1}), the decay rate k_2 is directly proportional to the emission, most notably for the smaller core diameters.

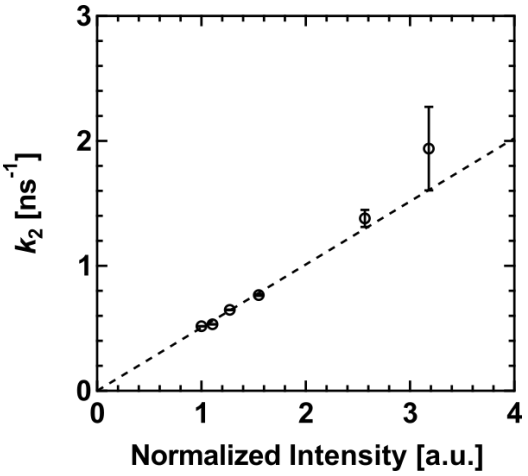

Fig. 5: Plot of the relaxation rate constant k_2 as a function of the normalized emission intensity. The dashed line is a linear fit to the data.

We propose that the measured emission properties of the dye-infiltrated sample are affected by several effects. Firstly, the pronounced increase in fluorescence with increasing size of the plasmonic particles is clearly the result of near-field enhancement and this effect becomes more pronounced for larger particles. To support this conclusion we have calculated electric field maps for differently sized particles using finite difference time domain software (FDTD). The results can be found in the Supporting Information, **Figures S7** and **S8**. Indeed the near-field strength and range increase significantly with increasing particle size. The fact that we observe a pronounced fluorescence enhancement implies that a significant fraction of the dye molecules is located in the near-field zone of the respective particles. **Figure S9** illustrates the structure of the core/shell particles adsorbed on the solid supports for different core sizes schematically. Due to the relatively large

footprint of the PNIPAM shell there will be a large range of possible dye-metal NP distances assuming homogeneous infiltration of the shell with Atto 488. This makes a quantitative analysis of the radiative and non-radiative rates impossible. However, since the near-field zone extends for several tens of nanometres for the larger plasmonic particles and thus includes a large volume fraction of the hydrogel shell, a significant fraction of the dyes will be located in the near-field regime. At the same time dye molecules will be located in the very close proximity to the metal NP surface. In this regime the dye emission is expected to be quenched.[33] However, the apparent correlation between the fluorescence lifetime and fluorescence intensity, shown in **Figure 5,** is an indication for the dominating effect of radiative over non-radiative processes. Whereas the fluorescence lifetime will shorten if either the non-radiative or the radiative decay rate increases, only an increase of the latter will result in enhanced fluorescence intensity. We can therefore assume that the fluorescence quantum yield improves with increasing particle size. Apart from these two effects, we also expect a small fraction of the infiltrated dye molecules to be located outside the near-field zone, far away from the metal surface. For this fraction we expect the fluorescence intensity and lifetime to be independent of the metal NP size. We want to emphasize that although we deal with multiple effects affecting the fluorescence of our probe molecules, the dominating effect is a strong near-field enhancement. We have been able to measure this enhancement systematically and its dependence on the plasmonic NP size using standard far-field spectroscopy on a single gradient sample. This is an important step towards understanding and probing plasmon-emitter interactions on the basis of a robust screening platform.

Conclusions

We have demonstrated a simple and robust method for creating plasmonic gradients of silver nanoparticles with continuously increasing particle size on a single substrate. The synthesis is highly controlled and reproducible. The procedure is based on seed-mediated overgrowth of particles assembled into non-close packed monolayers on a macroscopic substrate. By using a PNIPAM hydrogel shell as a spacer between the particles we have achieved well-defined inter-particle distances and hexagonal near-order. Thus, changes in absorption of light by the particle monolayers are only related to changes in the particle size. The UV-Vis spectra show a continuous increase in LSPR intensity along with a decrease in the FWHM for increasing particle size.

The PNIPAM shell has been infiltrated with Atto 488 in order to screen the effect of plasmonic particle size on the emission behavior of the dye. We have observed a threefold enhancement in the emission intensity of the dye with increasing particle size. Simultaneously, there is a decrease in the fluorescence lifetime. The decay rate varies proportionally with the emission intensity, leading us to conclude that the emission is enhanced by the plasmonic near-field due to the increased rate of excitation. The observed ultra-fast decay component suggests that some of the dye molecules experience fast non-radiative quenching.

With our plasmonic gradients we have presented a convenient platform to probe plasmonic properties and plasmon-emitter interactions by standard spectroscopic techniques on a single screening substrate.

Experimental Section

5.1. Materials

N,N'-Methylenebisacrylamide (99%), potassium peroxydisulfate (99%), ascorbic acid (>99%), trisodium citrate (99%), 3-butenylamine hydrochloride (97%), gold(III)-chloride hydrate (99.999% trace metal basis), sodium dodecylsulfate (99%) were purchased from Sigma-Aldrich. Glycine (99%) was purchased from Grüssing. Atto 488 NHS-ester was purchased from Atto-Tec. All chemicals were used as received. Analytical grade solvents were used for syntheses. Milli-Q water (Millipore, 18.2 MΩcm) was used for all syntheses, cleaning and sample preparation procedures. Glassware was cleaned with aqua regia and rinsed with Milli-Q water before use. Microscopy slides (soda-lime glass, 76 mm × 26 mm, Menzel) were cleaned using freshly prepared RCA-1 solution, stored in Milli-Q water, and thoroughly rinsed with water and ethanol before use.

5.2. Synthesis of butenylamine-functionalized gold nanospheres

AuNPs were prepared according to a modified Turkevich synthesis. Briefly, 300 mL of gold(III)-chloride solution (0.05 mM) were heated until boiling and 15 mL of pre-heated trisodium citrate solution (1 wt%) were added under vigorous stirring. After boiling for 20 minutes, the dispersion was allowed to cool down and 1.7 mL of SDS solution (1 mM) were added. 20 minutes later, 1.3 mL of an ethanolic 3-butenylamine hydrochloride solution (1.24 mM) were added. The AuNPs were purified by centrifugation at 1400*g* rcf overnight.

5.3. Synthesis of Au-PNIPAM core/shell microgels

100 mL of Milli-Q water were heated to 80 °C and purged with N_2 for 20 minutes. *N*-isopropylacrylamide (227 mg, 0.2 mmol) and *N,N*'-methylenebisacrylamide (53 mg, 0.34 mmol) were dissolved in small portions of Milli-Q water and added. 5.24 mL of AuNP stock solution ($c = 2.23 \cdot 10^{13}$ particles/mL)[34, 35] were added and the dispersion was

stirred for two minutes. 50 µL of 3-butenylamine hydrochloride (1.24 mM in ethanol) were added. After four minutes the polymerization was initialized by addition of 2 mL of aqueous potassium peroxydisulfate solution (2 mg/mL). The reaction was stopped after two hours by removal of the heating bath. The cool dispersion was purified by four centrifugation/redispersion cycles at 7500*g* rcf and lyophilized for long term storage.

5.4. Preparation of substrate-supported monolayers of Au-PNIPAM core/shell microgels

Freshly cleaned microscopy slides were again rinsed with Milli-Q water and dried using compressed air. They were placed on the recessed PTFE chuck of the spin coater (SCS G3, Specialty Coating Systems Inc.) and 200 µL of a 0.25 wt% aqueous dispersion of Au-PNIPAM core/shell microgels were evenly distributed on the surface. Please refer to SI for details on the speed program used for coating. The substrates were placed on a hot plate set to 200 °C for 5 min in order to cure the monolayer, rinsed with ethanol and Milli-Q water, and dried using compressed air.

5.5. Preparation of plasmonic gradients via seed-mediated silver overgrowth

The glass substrates carrying monolayers of Au-PNIPAM core/shell microgels were thoroughly rinsed with water and the backside of the substrate was swabbed with lint-free paper soaked with acetonitrile. 50 mL of ethanol and 40 mL of Milli-Q water were mixed in a 100 mL glass beaker equipped with a magnetic stirrer bar and cooled down in an ice bath. 3 mL of aqueous glycine solution (1 M) were added. The glass substrate was then clamped in the holder of the dip-coater. While stirring vigorously, 100 µL of $AgNO_3$ (15 mM in acetonitrile) and 100 µL of ascorbic acid (10 mM aqueous solution) were added dropwise. After stirring for 20 s the stirring speed was reduced to approx. 60 rpm. The substrate was then quickly lowered into the solution to the desired depth and retraction at a rate of 1 mm/min was initiated immediately. Once the substrate was fully withdrawn

from the solution, it was rinsed thoroughly with Milli-Q water and the backside of the substrate was swabbed with acetonitrile.

For fluorescence enhancement measurements the plasmonic gradient was covered with an excess of Atto 488-NHS solution (0.4 mg/mL in DMSO) and left under a petri dish for an hour. The excess solution was taken up using a plastic pipette, residues were blown off with compressed air and the substrate was dried on a hotplate set to 150 °C for 2 min.

5.6. Atomic force microscopy

Atomic force microscopy (AFM) was used to evaluate the homogeneity and degree of order of particle monolayers. We used a Veeco NanoScope 4 AFM equipped with OTESPA-R3 cantilevers (300 kHz, tetrahedral tip) by Bruker, operated in tapping mode at a line rate of 0.5 . In a typical measurement, several 30 µm× 30 µm scans of a sample were performed in 10 mm distance along the center axis of the glass slides.

5.7. Electron microscopy

Samples of Turkevich AuNPs and Au-PNIPAM core/shell microgels, were prepared by dispensing a small volume of the particles in water onto a carbon-coated copper grid (200 µm mesh) and letting the dispersant evaporate at room temperature. The samples were then characterized by transmission electron microscopy (TEM), using a Zeiss CEM902 microscope operated at 80 kV.

Plasmonic gradients were characterized by scanning electron microscopy (SEM) using a Zeiss LEO 1530 electron microscope operated at 3 kV and using the in-lens detector. The large gradient substrates were cut into small pieces of ca. 4 mm × 4 mm, fixed on holders and sputtered with a 1.3 nm Pt layer for better conductivity. Scans were performed on multiple areas of the samples in order to account for the sample inhomogeneity caused by the particle size gradient.

5.8. Optical characterization of plasmonic gradients

UV-Vis spectra were measured using the SPECORD 250 Plus spectrometer and WinAspect software by Analytik Jena. The glass slides carrying the plasmonic gradients are clamped into the sample holder so that the incident beam first passed the monolayer and then the substrate under an angle of 90°. A 2 mm wide slit aperture was positioned behind the substrate to decrease the analyzed spot size.

Fluorescence measurements were carried out on an Edinburgh Instruments FLS 980 spectrometer equipped with a Xe lamp and a pulsed Fianium WhiteLase supercontiuum laser as light sources, PMT detector for steady state, and a MCP detector for time resolved measurements. The angle between excitation and emission optics is 90° and sample holder is rotated by 45° compared to normal incidence. In order to prevent the reflected excitation beam from entering the emission optics, the sample is also tilted upwards by 45°. Due to this geometry, the effective illumination and detection angle is approx. 35°. The excitation wavelength and bandwidth were 450 nm and 15 nm respectively. The emission bandwidth was 6 nm.

Acknowledgements

The authors acknowledge financial support by the German Academic Exchange service (DAAD) through its Thematic Network Melbourne-Bayreuth Polymer/Colloid Network sponsored from funds of the Federal Ministry of Education and Research (BMBF). M.K. and J.S. want to acknowledge the German Research Foundation (DFG) for funding through the Emmy Noether programme under grant KA3880/1-1. P.M. thanks the ARC for support through CE170100026.

References

(1) Kreibig, U.; Vollmer, M. *Optical Properties of Metal Clusters*; Springer-Verlag Berlin Heidelberg1995.

(2) Liz-Marzán, L. M. Tailoring Surface Plasmons through the Morphology and Assembly of Metal Nanoparticles. *Langmuir* **2006,** *22* (1), 32-41.

(3) Rodríguez-Fernández, J.; Pérez-Juste, J.; García de Abajo, F. J.; Liz-Marzán, L. M. Seeded growth of submicron Au colloids with quadrupole plasmon resonance modes. *Langmuir* **2006,** *22* (16), 7007–7010.

(4) Evanoff, D. D.; Chumanov, G. Size-controlled synthesis of nanoparticles. 2. Measurement of extinction, scattering, and absorption cross sections. *J. Phys. Chem. B* **2004,** *108* (37), 13957-13962.

(5) Honold, T.; Volk, K.; Rauh, A.; Fitzgerald, J. P. S.; Karg, M. Tunable plasmonic surfaces via colloid assembly. *J. Mater. Chem. C* **2015,** *3* (43), 11449-11457.

(6) Evanoff Jr., D. D.; Chumanov, G. Synthesis and Optical Properties of Silver Nanoparticles and Arrays. *ChemPhysChem* **2005,** *6* (7), 1221-1231.

(7) Mulvaney, P. Surface plasmon spectroscopy of nanosized metal particles. *Langmuir* **1996,** *12* (3), 788-800.

(8) Novo, C.; Funston, A. M.; Pastoriza-Santos, I.; Liz-Marzan, L. M.; Mulvaney, P. Influence of the medium refractive index on the optical properties of single gold triangular prisms on a substrate. *J. Phys. Chem. C* **2008,** *112* (1), 3-7.

(9) Volk, K.; Fitzgerald, J. P. S.; Ruckdeschel, P.; Retsch, M.; König, T. A. F.; Karg, M. Reversible Tuning of Visible Wavelength Surface Lattice Resonances in Self-Assembled Hybrid Monolayers. *Adv. Opt. Mater.* **2017,** *5* (9), 1600971.

(10) Funston, A. M.; Novo, C.; Davis, T. J.; Mulvaney, P. Plasmon Coupling of Gold Nanorods at Short Distances and in Different Geometries. *Nano Lett* **2009,** *9* (4), 1651-1658.

(11) Volk, K.; Fitzgerald, J. P. S.; Retsch, M.; Karg, M. Time-Controlled Colloidal Superstructures: Long-Range Plasmon Resonance Coupling in Particle Monolayers. *Adv. Mater.* **2015,** *27* (45), 7332-7337.

(12) Singh, C. R.; Honold, T.; Gujar, T. P.; Retsch, M.; Fery, A.; Karg, M.; Thelakkat, M. The role of colloidal plasmonic nanostructures in organic solar cells. *Phys. Chem. Chem. Phys.* **2016,** *18* (33), 23155-23163.

(13) Zia, R.; Schuller, J. A.; Chandran, A.; Brongersma, M. L. Plasmonics: the next chip-scale technology. *Mater. Today* **2006,** *9* (7), 20-27.

(14) Karg, M.; König, T. A. F.; Retsch, M.; Stelling, C.; Reichstein, P. M.; Honold, T.; Thelakkat, M.; Fery, A. Colloidal self-assembly concepts for light management in photovoltaics. *Mater. Today* **2015,** *18* (4), 185-205.

(15) Contreras-Cáceres, R.; Pastoriza-Santos, I.; Alvarez-Puebla, R. A.; Pérez-Juste, J.; Fernández-Barbero, A.; Liz-Marzán, L. M. Growing Au/Ag Nanoparticles within Microgel Colloids for Improved Surface-Enhanced Raman Scattering Detection. *Chem. Eur. J.* **2010,** *16* (31), 9462–9467.

(16) Li, Z.-Y.; Xia, Y. Metal Nanoparticles with Gain toward Single-Molecule Detection by Surface-Enhanced Raman Scattering. *Nano Lett* **2010,** *10* (1), 243-249.

(17) Zhou, W.; Dridi, M.; Suh, J. Y.; Kim, C. H.; Co, D. T.; Wasielewski, M. R.; Schatz, G. C.; Odom, T. W. Lasing action in strongly coupled plasmonic nanocavity arrays. *Nat. Nanotechnol.* **2013,** *8*, 506-511.

(18) Lalisse, A.; Tessier, G.; Plain, J.; Baffou, G. Quantifying the Efficiency of Plasmonic Materials for Near-Field Enhancement and Photothermal Conversion. *J. Phys. Chem. C* **2015,** *119* (45), 25518–25528.

(19) Guzatov, D. V.; Vaschenko, S. V.; Stankevich, V. V.; Lunevich, A. Y.; Glukhov, Y. F.; Gaponenko, S. V. Plasmonic Enhancement of Molecular Fluorescence near Silver Nanoparticles: Theory, Modeling, and Experiment. *J. Phys. Chem. C* **2012,** *116* (19), 10723-10733.
(20) Bastús, N. G.; Comenge, J.; Puntes, V. Kinetically Controlled Seeded Growth Synthesis of Citrate-Stabilized Gold Nanoparticles of up to 200 nm: Size Focusing versus Ostwald Ripening. *Langmuir* **2011,** *27* (17), 11098-11105.
(21) Pazos-Perez, N.; Garcia de Abajo, F. J.; Fery, A.; Alvarez-Puebla, R. A. From Nano to Micro: Synthesis and Optical Properties of Homogeneous Spheroidal Gold Particles and Their Superlattices. *Langmuir* **2012,** *28* (24), 8909-8914.
(22) Evanoff, D. D.; Chumanov, G. Size-controlled synthesis of nanoparticles. 1. "Silver-only" aqueous suspensions via hydrogen reduction. *J. Phys. Chem. B* **2004,** *108* (37), 13948-13956.
(23) Bastús, N. G.; Merkoçi, F.; Piella, J.; Puntes, V. Synthesis of Highly Monodisperse Citrate-Stabilized Silver Nanoparticles of up to 200 nm: Kinetic Control and Catalytic Properties. *Chem. Mater.* **2014,** *26* (9), 2836-2846.
(24) Hummel, P.; Lerch, A.; Goller, S. M.; Karg, M.; Retsch, M. Simple and High Yield Synthesis of Metal-Polymer Nanocomposites: The Role of Theta-Centrifugation as an Essential Purification Step. *Polymers* **2017,** *9* (12), 659.
(25) Ebeling, B.; Vana, P. RAFT-Polymers with Single and Multiple Trithiocarbonate Groups as Uniform Gold-Nanoparticle Coatings. *Macromolecules* **2013,** *46* (12), 4862-4871.
(26) Rauh, A.; Honold, T.; Karg, M. Seeded precipitation polymerization for the synthesis of gold-hydrogel core-shell particles: the role of surface functionalization and seed concentration. *Colloid Polym. Sci.* **2016,** *294* (1), 37-47.
(27) Müller, M. B.; Kuttner, C.; König, T. A. F.; Tsukruk, V. V.; Förster, S.; Karg, M.; Fery, A. Plasmonic library based on substrate-supported gradiential plasmonic arrays. *ACS Nano* **2014,** *8* (9), 9410–9421.
(28) Karg, M.; Jaber, S.; Hellweg, T.; Mulvaney, P. Surface Plasmon Spectroscopy of Gold−Poly-N-isopropylacrylamide Core−Shell Particles. *Langmuir* **2011,** *27* (2), 820-827.
(29) Hada, H.; Yonezawa, Y.; Yoshida, A.; Kurakake, A. Photoreduction of silver ion in aqueous and alcoholic solutions. *J. Phys. Chem.* **1976,** *80* (25), 2728-2731.
(30) Sánchez-Iglesias, A.; Aldeanueva-Potel, P.; Ni, W.; Pérez-Juste, J.; Pastoriza-Santos, I.; Alvarez-Puebla, R. A.; Mbenkum, B. N.; Liz-Marzán, L. M. Chemical seeded growth of Ag nanoparticle arrays and their application as reproducible SERS substrates. *Nano Today* **2010,** *5* (1), 21–27.
(31) Anger, P.; Bharadwaj, P.; Novotny, L. Enhancement and Quenching of Single-Molecule Fluorescence. *Phys. Rev. Lett.* **2006,** *96* (11), 113002.
(32) Walhorn, V.; Paskarbeit, J.; Frey, H. G.; Harder, A.; Anselmetti, D. Distance dependence of near-field fluorescence enhancement and quenching of single quantum dots. *Beilstein J. Nanotechnol.* **2011,** *2*, 645-652.
(33) Reineck, P.; Gómez, D.; Ng, S. H.; Karg, M.; Bell, T.; Mulvaney, P.; Bach, U. Distance and wavelength dependent quenching of molecular fluorescence by Au@SiO2 core-shell nanoparticles. *ACS Nano* **2013,** *7* (8), 6636–6648.
(34) Hendel, T.; Wuithschick, M.; Kettemann, F.; Birnbaum, A.; Rademann, K.; Polte, J. In Situ Determination of Colloidal Gold Concentrations with UV–Vis Spectroscopy: Limitations and Perspectives. *Anal. Chem.* **2014,** *86* (22), 11115-11124.
(35) Honold, T.; Skrybeck, D.; Wagner, K. G.; Karg, M. Fully Reversible Quantitative Phase Transfer of Gold Nanoparticles Using Bifunctional PNIPAM Ligands. *Langmuir* **2017,** *33* (1), 253-261.

TOC

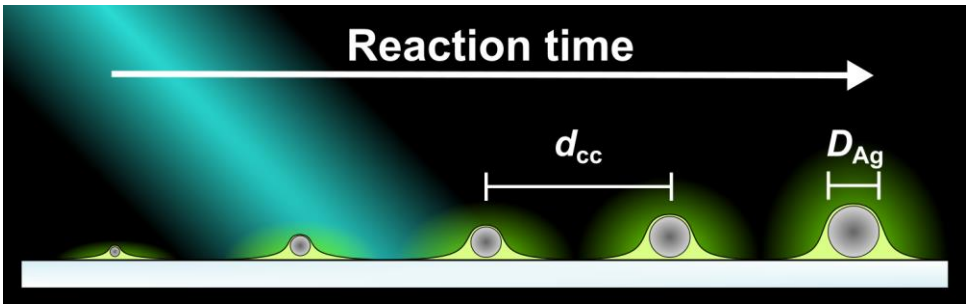

Schematic representation of the silver particle size gradient on a glass substrate. The grey circles represent the Ag@Au core particles, embedded in a dye-loaded, hydrogel shell (light green). The particles are assembled in a hexagonal lattice with a nearest-neighbor distance d_{cc} using the hydrogel shell as spacer. The sample is irradiated with blue-green light. The emission intensity increases with particle size, indicated by the green halos around the particles.